ORIGINAL PAPER

Polyphase strain caps

Tamer Abu-Alam · Kurt Stüwe

Abstract Strain caps are one of a series of microstructures that typically form during deformation of a softer matrix around hard objects. However—in contrast to other microstructures around porphyroblasts, for example pressure shadows—strain caps are rarely described in the literature. Here we describe strain caps with particular focus on strain caps associated with growth of a new phase, not elsewhere present in the paragenesis. Examples from foliated, amphibolite facies, metapelitic schists from Alaska, Sinai and Bhutan are discussed. All examples show chlorite growth exclusively in strain caps formed around porphyroblasts. Porphyroblasts around which the strain caps grow are muscovite, staurolite and garnet, respectively. In all of these examples strain caps formed synkinematically, but the chlorite grew statically at a later stage. Three mechanisms can explain the formation of new phases in the strain cap region: (a) the strain cap region may have experienced different *P-T* conditions from the matrix; (b) the strain cap region has a different effective bulk composition from the surrounding matrix; (c) fluid flow that is preferentially focused parallel to the foliation planes causing only local adjustment to retrograde metamorphism in the strain cap region. We show that the third hypothesis is the most preferable mechanism. Indeed, the absence of chlorite outside the strain cap region allows a quantification of the amount of fluid that infiltrated the rock. It is shown that for Bhutan sample about 8.5 mole% more water must have been added to the rock during fluid infiltration to cause the strain cap formation.

T. Abu-Alam (✉) · K. Stüwe
Institut für Erdwissenschaften, Universität Graz,
Universitätsplatz 2,
8010 Graz, Austria
e-mail: tamer.abu-alam@uni-graz.at

Introduction

Strain caps are one of a series of microstructures that typically form during deformation of a softer matrix around hard objects (e.g. porphyroblasts and-clasts). As such, they can be used to infer aspects of the stress and strain fields around the porphyroblasts. Other microstructural elements around pophyroblasts include their strain- and pressure shadows, as well as the line that effectively separates the flow around the porphyroblast from the "eddy-flow" in the strain shadow: the separatrix (Fig. 1a). Some of these microstructural elements bear characteristic information on the vorticity of the stress field and have—therefore—received a lot of attention in the literature. For example, the orientation of a pressure shadow with respect to the flow lines is a direct consequence of the ratio of pure- to simple shear and can thus be used to estimate the vorticity (Fig. 1b, c and d). A GEOREF search lists more than 36 entries for the term "pressure shadow" or "strain shadow" in the title of a paper (e.g. Takagi and Ito 1988; Etchecopar and Malavieille 1987; Tenczer et al. 2001). In contrast, strain caps are barely described outside their definition (e.g. Passchier and Trouw 1996, 2005), possibly because strain caps are considered to merely reflect the denser flow lines around the porphyroblast without much additional significance for the orientation of the stress field. Typically, strain caps are evidenced by a region that is depleted in quartz and enriched in micas occurring on opposite sides of the rigid body, in the quarters orthogonal to the strain shadow. In one of the few studies that have discussed strain caps, Trouw et al. (2008) showed this orthogonal relationship between strain cap and strain shadow may be responsible for the orthogonal arrangement of spiral inclusion trails in garnet. They argue that synkinematically grown garnet typically grows preferentially in direction of the strain cap
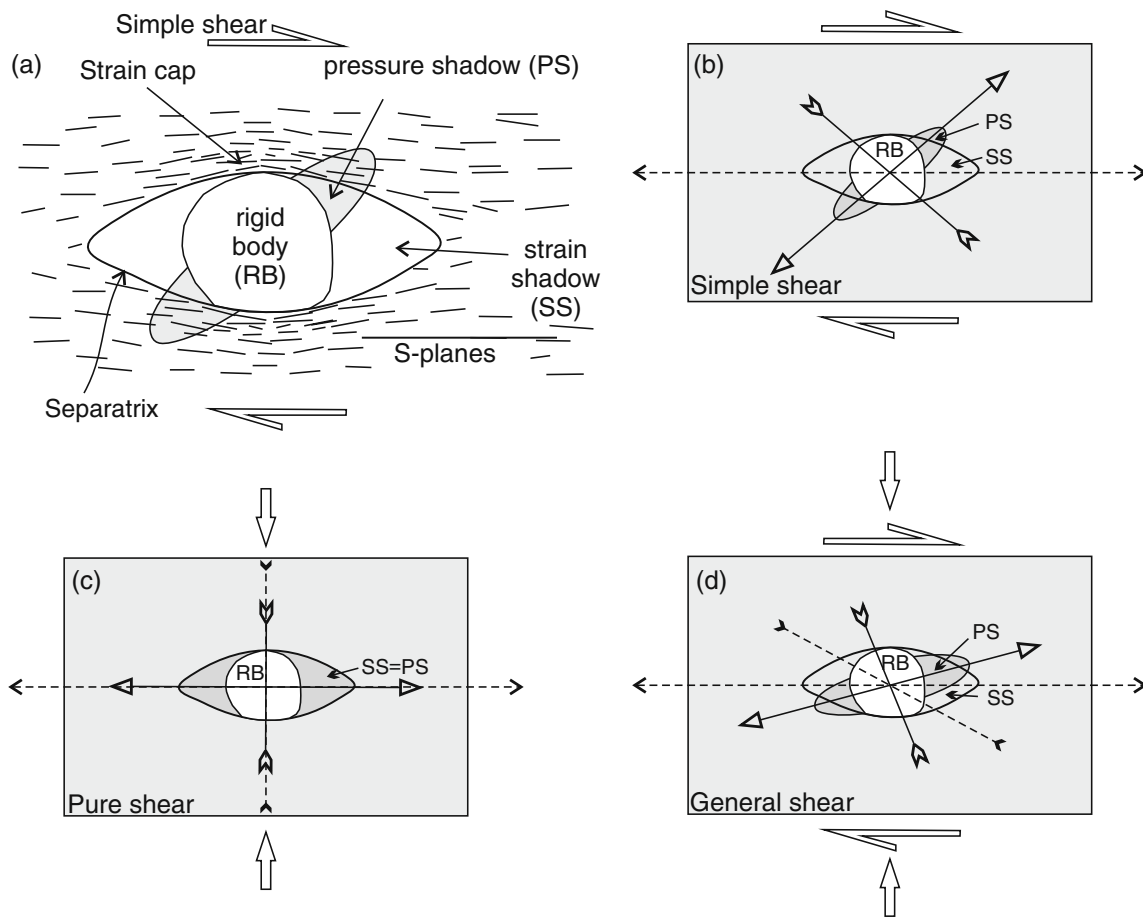
Fig. 1 Microstructural elements around rigid objects-(**a**) shows the names of different structural elements (modified after Passchier and Trouw 2005). (**b**), (**c**) and (**d**) show the geometric changes of these elements in response to simple shear, pure shear and general shear, respectively. *Dashed arrows* show the eigenvectors of the flow field. *Continuous arrows* show the orientations of the instantaneous stretching axes

as this region is concentrated in the nutrient cations. As the porphyroblast continues to elongate in direction of the strain cap by growth, it eventually rotates into the direction of the fabric attractor, before continuing to grow on its sides towards the new strain cap.

In this paper we describe strain caps with the opposite relationship: Not preferential porphyroblast growth, but preferential consumption of the porphyroblasts in the region of the strain cap. This process leads to reaction and formation of new phases (typically chlorite) that grow exclusively in the strain cap region. Such a microstructure can obviously not be explained through deformation alone, but requires an intergraded interpretation in terms of the metamorphic reaction in relationship to the deformation. Here we use detailed microstructural description, petrographic work and thermodynamic modeling to explain formation mechanism of new phases grown in the strain cap region. We shall show that these polyphase strain caps can only form due to post metamorphic peak fluid

infiltration through matrix foliation and we quantify the amount of water that is required for their formation.

Geological setting

The strain caps of our interest show chlorite growth in the strain cap region surrounding various types of porphyroblasts. Interestingly, we have discovered this feature in a series of amphibolite facies metamorphic rocks from different locations. Here, we present our interpretation for samples from three different regions: Bhutan, Sinai and Alaska.

The Bhutan samples which will be studied here are pelitic schist samples from the Higher Himalaya Crystalline and are part of a suite of samples that were collected by Stüwe and Foster (2001). The Higher Himalayan Crystalline is a high grade complex located at the Himalayan front between two major crustal scale shear zones, the Main

Central Thrust (MCT) and the South Tibetan Detachment Zone (STDZ). The MCT is one of the major features associated with the collision between the Indoaustralian and the Asian continental plates. It is associated with inverted metamorphic isograds both above—in Higher Himalaya Crystalline rocks (amphibolites facies) and below—in Lesser Himalaya rocks (greenschist facies) (e.g. Gansser 1964; Le Fort 1975; Hodges et al. 1988; Hubbard 1989; Vannay and Hodges 1996; Grujic et al. 1996). The Lesser Himalaya rocks are separated from Sub-Himalayan domain (mollase type deposits) in the south by the Main Boundary Thrust (MBT). The main movement on the MCT occurred at about 15–22.5 Ma (e.g. Hubbard and Harrison 1989; Hodges et al. 1996) and it was synchronous with the prograde metamorphism (Grujic et al. 1996). The Higher Himalaya Crystalline rocks show a wide variation of pressure-temperature conditions (500–800°C and 4.8–8.5 kbar; e.g. Dasgupta et al. 2004). However, the transect that was studied by Stüwe and Foster (2001) shows peak conditions in the range of 600–650°C at 6.5 kbar. Granitic magmas originated by the melting of the Higher Himalayan Crystalline pelitic gneisses by infiltration of fluid at the time of thrusting along the MCT. These magmas intruded later in the higher crust rocks as leucogranite bodies (Le Fort 1981; Vidal et al. 1982; France-Lanord and Le Fort 1988; England et al. 1992).

Sinai samples are from Taba metamorphic complex which is directly located to the northwest of the Gulf of Aqaba and consists of metapelitic schists, migmatites, metagabbro-diorites, orthogneisses, and metamorphosed mafic dykes (Kröner et al. 1990; Heimann et al. 1995; Cosca et al. 1999; Abu El-Enen et al. 1999, 2004; Eliwa et al. 2008). Abu El-Enen et al. (2004) identified four metamorphic zones in the metapelites; garnet, staurolite, staurolite-sillimanite and staurolite-cordierite zones. The samples which will be studied here are from the staurolite zone. The entire metamorphic complex underwent polyphase deformation with three ductile phases D_1-D_3 (e.g. Shimron 1980) accompanied by a single metamorphic event with peak condition (590–640°C and 5–6 kbar; e.g. Abu El-Enen et al. 2004) followed by a brittle D_4 phase. Cosca et al. (1999) concluded that regional metamorphism at 620±10 Ma of the complex is related to the collision of greater east and west Gondwanaland. Subsequent to the peak metamorphism and during the exhumation, the metamorphic sequences of Sinai were intruded by post-tectonic granites and the equivalent volcanic rocks (e.g. Abu-Alam and Stüwe 2009a) and were affected by fluid influx (Abu-Alam et al. 2010).

The Alaska samples which will be studied here are pelitic schists from the rim of the Chugach Metamorphic Complex. This complex is an Eocene metamorphic complex in southern Alaska related to the subduction of the Pacific plate underneath the North American continent (Sisson and Hollister 1988; Sisson et al. 1989). This complex is bound in the north by the Border Range fault and in the south by the Contact fault (e.g. Plafker et al. 1994). Hudson and Plafker (1982) were the first to study the tectonic evolution of this complex. Since this contribution the Chugach Metamorphic Complex is known to have symmetric geometry with a core made up of migmatitic gneiss and margins of schists. The studied samples are part of a suite that were collected by Bruand et al. (2010). Sisson and Hollister (1988) suggested around 3 kb as an average pressure value for the entire complex and temperatures of 550°C for the external schist zone and 650°C for the highest grade core of the complex. However, the recent study by Bruand et al. (2010) reveals that the complex shows a significant increase of pressure and temperature from the north (550°C-3 kbar) to the south (<750°C-13 kbar). Based on a detailed thermodynamic study of Bruand et al. (op cit), the lower crustal part of the complex (migmatitic gneiss) was subjected to H_2O-saturated melting process. This melt intruded later in the upper crustal rocks (schists) to form magmatic intrusion bodies e.g. Sanak-Baranof belt (Hill et al. 1981; Moore et al. 1983; Barker et al. 1992; Sisson et al. 2003; Farris and Paterson 2007; Farris and Paterson 2009).

Microstructural descriptions and metamorphic conditions

In the chosen three examples, chlorite bearing strain caps form around different porpyroblasts of garnet, staurolite and muscovite. The mineral assemblages in the studied samples were analysed at the Institute of Earth Science, Karl-Franzens-Universität Graz, Austria, using a JEOL JSM-6310 scanning electron microscope following standard procedures, operating in EDS/WDS mode at 5 nA beam current, accelerating voltage 15 kV and duration time is 100 s. The chemical formulae and end-members activities were calculated using the program AX (http://www.esc.cam.ac.uk/research/research-groups/holland/ax). The mineral abbreviations which will be used in the following sections are from Holland and Powell (1998). Pressure-temperature conditions (Tables 1, 2 and 3) were calculated by solving independent sets of reactions between mineral end-members (Appendix 1) by THERMOCALC 330 (Powell and Holland 1988) and the internally consistent dataset of Holland and Powell (1998).

Bhutan sample is a typical amphibolite facies garnet mica schist (Figs. 2a, b and 3a). The sample is composed of garnet, biotite, white mica, chlorite, quartz and sphene. Parallel mica and quartz crystals define the metamorphic foliation, which wraps around the garnet porphyroblasts

Table 1 Representative mineral analyses of Bhutan sample

Mineral	Strain shadow									Strain cap		
	g4	bi4	mu4	g5	bi5	mu5	g10	bi10	mu10	g7	bi7	chl7
SiO_2	37.75	34.49	47.13	37.49	36.41	45.83	38.46	36.39	46.75	37.22	35.8	23.87
TiO_2	0.14	3.21	0.77	0.22	2.56	0.53	0.15	2.31	0.44	0.24	3.28	0.3
Al_2O_3	20.4	17.99	36.58	21.05	18.42	34.51	21.22	18.44	35.2	20.77	19.19	21.43
Fe_2O_3	—	—	—	—	—	—	—	—	—	0.51	—	—
FeO	33.14	20.75	1.12	36.11	21.5	1.38	35.19	20.82	1.87	33.63	20.46	27.92
MnO	1.12	0.12	0.08	0.71	0.04	b.d.l.	1	0.14	b.d.l.	1.45	b.d.l.	0.17
MgO	1.12	7.91	0.55	1.77	7.86	0.68	1.69	8.82	0.83	1.17	8.39	11.51
CaO	6.15	b.d.l.	0.03	3.43	0.11	0.11	3.63	0.14	0.09	5.66	0.07	0.09
Na_2O	0.06	0.29	1.51	0.03	0.25	1.18	0.07	0.26	1.07	0.05	0.24	0.07
K_2O	0.1	9.88	9.96	b.d.l.	9.85	10.08	b.d.l.	10.22	10.29	0.02	10	0.24
Totals	99.98	94.64	97.84	100.83	97.04	94.33	101.44	97.54	96.56	100.73	97.49	85.59
O	12	11	11	12	11	11	12	11	11	12	11	14
Si	3.044	2.682	3.051	3.005	2.75	3.086	3.047	2.733	3.081	2.99	2.682	2.63
Ti	0.008	0.188	0.038	0.014	0.145	0.027	0.009	0.13	0.022	0.014	0.185	0.025
Al	1.939	1.649	2.792	1.989	1.64	2.74	1.982	1.633	2.734	1.967	1.695	2.784
Fe^{3+}	—	—	—	—	—	—	—	—	—	0.031	—	—
Fe^{2+}	2.235	1.349	0.061	2.421	1.358	0.078	2.332	1.308	0.103	2.259	1.282	2.573
Mn	0.077	0.008	0.004	0.048	0.002	—	0.067	0.009	—	0.099	—	0.015
Mg	0.135	0.917	0.054	0.212	0.884	0.068	0.2	0.987	0.082	0.14	0.937	1.891
Ca	0.532	—	0.002	0.294	0.009	0.008	0.308	0.011	0.006	0.487	0.006	0.01
Na	0.009	0.043	0.19	0.005	0.036	0.155	0.01	0.038	0.137	0.008	0.035	0.014
K	0.011	0.98	0.823	—	0.949	0.866	—	0.98	0.865	0.002	0.956	0.033
Sum	7.988	7.818	7.019	7.989	7.777	7.028	7.957	7.829	7.031	8	7.781	9.977
$X(chl) = Fe^{2+}/(Fe^{2+}+Mg^{2+})$												0.576
Activity of end-members												
py	0.00026			0.00074			0.00069			0.00027		
gr	0.0062			0.00124			0.0014			0.0046		
alm	0.37			0.5			0.44			0.41		
phl		0.0248			0.0261			0.034			0.0272	
ann		0.073			0.076			0.07			0.06	
east		0.03			0.026			0.033			0.034	
mu			0.69			0.71			0.69			
cel			0.025			0.017			0.015			
fcel			0.028			0.02			0.018			
pa			0.8			0.13			0.11			
clin												0.0106
daph												0.048
ames												0.0152
Pressure	7.2±0.8	7.2±0.8			7.1±0.5			6±0.7			7.2±0.5	
Temp.	614±30	614±30			564±45			513±35			557±50	

The chemical formulae were calculated based on the number of oxygen atoms listed in the table and ignoring H_2O for hydrated minerals. Activities of end members were calculated with the program AX. Average pressure and temperature values were calculated with THERMOCALC. Mineral analyses (mu1* and mu3*) are for mica grains along the chlorite cleavages. b.d.l is below detection limit.

Table 1 (continued)

Mineral	Strain cap										
	mu7	g9	bi9	chl9	mu9	g11	bi11	chl11	mu11	mu1*	mu3*
SiO_2	46.26	36.75	35.88	24.76	46.71	37.21	36.01	23.79	48.27	44.21	44.38
TiO_2	0.58	0.1	2.33	0.41	0.53	0.38	3.27	0.16	0.85	1.78	1.43
Al_2O_3	36.12	20.44	19.86	22.7	34.83	20.9	18.03	21.87	32.38	34.53	34.53
Fe_2O_3	–	2.11	–	–	–	0.92	–	–	–	–	–
FeO	1.18	31.72	20.62	27.77	1.51	30.3	20.91	27.66	1.79	1.06	1.08
MnO	b.d.l.	1.05	0.17	0.13	0.03	2.86	0.05	0.09	b.d.l.	0.06	b.d.l.
MgO	0.75	1.75	7.99	11.79	0.68	1.33	8.12	11.36	1.37	0.87	0.89
CaO	0.15	5.99	0.08	0.05	0.07	7.08	0.01	0.04	0.02	b.d.l.	0.08
Na_2O	1.45	0.09	0.26	0.04	1.37	0.04	0.28	0.02	0.84	0.78	0.78
K_2O	10.21	0.02	10.28	0.12	10.37	b.d.l.	10.01	0.12	10.27	11.04	11.19
Totals	96.75	99.85	97.52	87.76	96.13	100.94	96.71	85.17	95.93	94.35	94.37
O	11	12	11	14	11	12	11	14	11	11	11
Si	3.038	2.964	2.692	2.639	3.092	2.969	2.729	2.626	3.196	2.998	3.01
Ti	0.029	0.006	0.132	0.033	0.026	0.023	0.187	0.013	0.043	0.091	0.073
Al	2.797	1.943	1.757	2.853	2.718	1.966	1.611	2.846	2.527	2.761	2.761
Fe^{3+}	–	0.128	–	–	–	0.055	–	–	–	–	–
Fe^{2+}	0.065	2.14	1.294	2.475	0.083	2.023	1.325	2.553	0.099	0.06	0.061
Mn	–	0.072	0.011	0.011	0.001	0.193	0.003	0.008	–	0.003	–
Mg	0.073	0.211	0.894	1.873	0.067	0.158	0.917	1.869	0.135	0.088	0.09
Ca	0.011	0.518	0.006	0.005	0.005	0.606	0.001	0.005	0.001	–	0.006
Na	0.184	0.014	0.038	0.008	0.176	0.006	0.041	0.004	0.107	0.102	0.102
K	0.856	0.002	0.984	0.016	0.876	–	0.968	0.018	0.868	0.955	0.969
Sum	7.055	8	7.809	9.914	7.048	8	7.783	9.946	6.983	7.06	7.072
$X(chl) = Fe^{2+}/(Fe^{2+}+Mg^{2+})$				0.569				0.577			
Activity of end-members											
py		0.00096				0.00046					
gr		0.0053				0.0093					
alm		0.34				0.29					
phl			0.0296				0.0256				
ann			0.065				0.07				
east			0.034				0.028				
mu	0.68				0.72				0.63	0.75	0.73
cel	0.034				0.019				0.037	0.019	0.033
fcel	0.03				0.024				0.027	0.013	0.023
pa	0.86				0.14				0.078	0.08	0.578
clin				0.0115				0.0109			
daph				0.046				0.051			
ames				0.0146				0.0147			
Pressure			6.9±0.4				7.2±0.6				
Temp.			627±25				600±40				

Table 2 Representative mineral analyses of Sinai sample

Mineral	Strain shadow								Strain cap									
	bi1	mu1	fsp1	st1	bi2	mu2	fsp2	st2	bi7	chl7	mu7	fsp7	st7	bi9	chl9	mu9	fsp9	st9
SiO_2	34.22	45.31	61.88	27.08	33.91	45.34	62.01	26.29	33.61	24.18	44.49	62.59	27.89	33.61	24.57	44.7	62.68	27.34
TiO_2	3.07	0.97	0.09	1.1	2.37	0.83	b.d.l.	1.26	3.48	0.07	0.71	b.d.l.	1.07	5.22	0.34	1.04	0.05	1.09
Al_2O_3	19.59	35.11	22.82	51.98	19.82	36.08	23.82	51.05	19.14	21.39	35.85	23.37	53.45	17.43	20.92	34.96	23.6	52.97
Fe_2O_3	–	–	–	–	–	–	–	–	–	–	–	–	–	–	–	–	–	–
FeO	17.36	1.11	b.d.l.	12.91	18.79	1.1	b.d.l.	12.04	19.25	25.07	1.09	b.d.l.	12.24	19.18	24.8	2.09	b.d.l.	11.89
MnO	0.1	b.d.l.	b.d.l.	0.4	0.1	0.02	0.05	0.38	0.14	0.2	0.03	0.02	0.44	0.13	0.24	0.01	b.d.l.	0.38
MgO	8.52	0.52	0.09	1.61	8.18	0.85	0.26	1.43	8.67	12.61	0.19	b.d.l.	1.36	7.43	13.47	0.9	0.12	1.03
CaO	0.08	0.06	5.29	b.d.l.	0.06	0.13	5.47	0.05	0.04	0.07	0.14	5.13	0.05	0.27	0.06	0.07	5.36	b.d.l.
Na_2O	0.2	0.93	9.36	b.d.l.	0.11	1.28	9.3	0.04	0.13	b.d.l.	0.99	9.17	0.02	0.16	0.01	0.72	9.54	0.02
K_2O	10.05	10.34	0.11	b.d.l.	10.28	10.34	0.11	0.01	9.24	0.01	10.68	0.11	b.d.l.	10.09	0.03	10.38	0.11	b.d.l.
Totals	93.24	94.5	99.65	95.08	93.71	95.98	101.06	92.57	93.73	83.59	94.22	100.47	96.54	93.62	84.45	94.98	101.46	94.74
O	11	11	8	46	11	11	8	46	11	14	11	8	46	11	14	11	8	46
Si	2.656	3.047	2.758	7.724	2.641	3.006	2.731	7.684	2.612	2.68	3.009	2.762	7.793	2.639	2.692	3.009	2.745	7.771
Ti	0.179	0.049	0.003	0.237	0.139	0.042	–	0.277	0.203	0.006	0.036	–	0.224	0.308	0.028	0.053	0.002	0.232
Al	1.792	2.783	1.199	17.479	1.82	2.82	1.237	17.59	1.754	2.795	2.859	1.216	17.606	1.613	2.703	2.774	1.218	17.751
Fe^{3+}	–	–	0.007	–	–	–	0.003	–	–	–	–	0.006	–	–	–	0.005	0.008	–
Fe^{2+}	1.127	0.063	–	3.079	1.224	0.061	–	2.944	1.251	2.324	0.062	–	2.86	1.259	2.273	0.117	–	2.828
Mn	0.007	–	–	0.097	0.007	0.001	0.002	0.095	0.009	0.018	0.002	0.001	0.104	0.009	0.022	0.001	–	0.09
Mg	0.985	0.052	0.006	0.684	0.949	0.084	0.017	0.623	1.004	2.083	0.019	–	0.566	0.869	2.2	0.09	0.008	0.436
Ca	0.006	0.004	0.252	–	0.005	0.009	0.258	0.017	0.003	0.009	0.01	0.242	0.015	0.023	0.007	0.005	0.252	–
Na	0.03	0.121	0.809	–	0.017	0.165	0.794	0.023	0.02	–	0.13	0.785	0.011	0.024	0.002	0.094	0.81	0.011
K	0.995	0.887	0.006	–	1.021	0.875	0.006	0.002	0.916	0.001	0.922	0.006	–	1.011	0.005	0.891	0.006	–
Sum	7.781	7.014	5.042	29.3	7.828	7.062	5.049	29.256	7.775	9.916	7.051	5.02	29.183	7.762	9.932	7.042	5.048	29.124
Ca(pl) = Ca/(Ca+Na+K)			0.23				0.24					0.23					0.24	
Activity of end-members																		
phl	0.034				0.0342				0.029					0.0173				
ann	0.04				0.054				0.05					0.057				
east	0.047				0.045				0.042					0.026				
an			0.39				0.4					0.39					0.39	
ab			0.76				0.76					0.77					0.76	
mst				0.0017				0.0015					0.0013					0.00061
fst				0.4				0.42					0.43					0.51
mu		0.74				0.72					0.79					0.68		
cel		0.02				0.014					0.0098					0.0151		
fcel		0.024				0.01					0.032					0.02		
pa		0.58				0.14					0.68					0.332		
clin										0.0194					0.022			
daph										0.034					0.027			
ames										0.0206					0.0246			
Pressure		6±0.8				6.2±0.5					6.1±0.3					6±0.7		
Temp.		652±30				649±25					643±40					635±33		

The chemical formulae were calculated based on the number of oxygen atoms listed in the table and ignoring H_2O for hydrated minerals. Activities of end members were calculated with the program AX. Average pressure and temperature values were calculated with THERMOCALC. b.d.l is below detection limit.

Table 3 Representative mineral analyses of Alaska sample

Mineral	Strain shadow									Strain cap											
	fsp6	bi6	mu6	fsp7	bi7	mu7	fsp9	bi9	mu9	fsp11	chl11	bi11	mu11	fsp12	chl12	bi12	mu12	fsp14	chl14	bi14	mu14
SiO_2	62.53	34.36	45.88	62.37	34.52	45.27	62.88	34.22	46.21	62.29	24.9	34.37	45.51	60.49	24.13	34.48	45.66	63.59	24.75	34.86	46.15
TiO_2	0.23	4.11	1.62	0.14	4.14	1.35	0.02	4.33	1.63	0.09	0.28	4.38	1.57	0.23	0.07	3.11	1.77	b.d.l.	0.33	4.25	1.88
Al_2O_3	23.13	18.04	34.35	23.56	18.46	34.95	23.9	17.62	35.99	23.75	21.22	18.39	35.16	24.68	21.28	17.87	35.08	23.22	21.41	18.15	35.32
Fe_2O_3	–		–	–		–								–			–	–			–
FeO	b.d.l.	19.3	1.19	b.d.l.	18.72	0.99	b.d.l.	19.38	1.17	b.d.l.	24.91	19.48	0.93	b.d.l.	24.42	18.71	1.19	b.d.l.	24.45	19.27	1.34
MnO	b.d.l.	0.3	b.d.l.	0.05	0.38	b.d.l.	0.06	0.42	0.04	b.d.l.	0.59	0.44	0.1	0.05	0.61	0.42	0.07	0.03	0.71	0.42	0.02
MgO	b.d.l.	8.46	1.1	0.22	8.62	0.9	0.01	8.3	0.87	b.d.l.	13.36	8.11	0.66	0.06	12.98	9.17	0.77	b.d.l.	13.5	8.77	1.08
CaO	5	0.04	0.19	5.36	0.1	0.04	5.54	0.06	b.d.l.	5.71	0.04	0.04	0.04	6.97	0.02	0.15	b.d.l.	5.1	b.d.l.	0.07	0.14
Na_2O	9.47	0.11	0.73	9.64	0.06	0.73	9.23	0.05	0.77	9.06	0.04	0.12	0.71	8.44	0.03	0.05	0.72	9.59	0.04	0.1	0.82
K_2O	0.12	10.38	11.09	0.13	10.4	11.12	0.13	10.27	11.22	0.11	b.d.l.	10.32	11.13	0.06	0.04	10.47	11.06	0.21	0.13	10.5	10.9
Totals	100.48	95.17	96.18	101.52	95.41	95.36	101.78	94.67	97.92	101.02	85.39	95.68	95.84	100.99	83.57	94.48	96.36	101.73	85.36	96.4	97.65
O	8	11	11	8	11	11	8	11	11	8	14	11	11	8	14	11	11	8	14	11	11
Si	2.76	2.649	3.048	2.737	2.646	3.029	2.747	2.656	3.013	2.739	2.7	2.637	3.029	2.676	2.674	2.674	3.026	2.774	2.682	2.652	3.018
Ti	0.008	0.238	0.081	0.005	0.239	0.068	0.001	0.253	0.08	0.003	0.023	0.253	0.079	0.008	0.006	0.181	0.088	–	0.027	0.243	0.092
Al	1.204	1.64	2.69	1.219	1.668	2.757	1.231	1.612	2.766	1.231	2.713	1.663	2.759	1.287	2.78	1.634	2.741	1.194	2.735	1.628	2.722
Fe^{3+}	0.009			0.002			0.001			0.007				0.001				0.007			
Fe^{2+}	–	1.244	0.066	–	1.2	0.055	–	1.258	0.064	–	2.259	1.25	0.052	–	2.263	1.213	0.066	–	2.216	1.226	0.073
Mn	–	0.019	–	0.002	0.025	–	–	0.027	0.002	–	0.054	0.029	0.006	0.002	0.057	0.028	0.004	–	0.065	0.027	0.001
Mg	–	0.972	0.108	0.014	0.985	0.09	0.002	0.96	0.085	–	2.159	0.928	0.066	0.004	2.144	1.06	0.076	0.001	2.18	0.994	0.105
Ca	0.236	0.003	0.014	0.252	0.008	0.003	0.259	0.005	0.097	0.269	0.005	0.004	0.003	0.33	0.003	0.012	–	0.238	0.009	0.006	0.01
Na	0.81	0.016	0.094	0.82	0.009	0.094	0.782	0.008	0.097	0.773	0.008	0.018	0.092	0.724	0.006	0.008	0.093	0.811	0.017	0.014	0.104
K	0.007	1.021	0.94	0.007	1.017	0.95	0.007	1.017	0.933	0.006	–	1.01	0.945	0.004	0.006	1.036	0.935	0.012	0.017	1.019	0.909
Sum	5.034	7.809	7.043	5.06	7.795	7.047	5.031	7.798	7.04	5.028	9.923	7.793	7.031	5.036	9.936	7.849	7.03	5.037	9.935	7.809	7.036
Activity of end-members																					
an	0.37			0.39			0.41			0.43				0.51				0.37			
ab	0.77			0.77			0.75			0.74				0.69				0.77			
mu			0.68			0.73			0.72				0.75				0.74				0.68
cel			0.04			0.032			0.025				0.027				0.017				0.019
fcel			0.025			0.02			0.019				0.021				0.014				0.013
pa			0.545			0.506			0.454				0.506				0.074				0.078
phl		0.026			0.028			0.025				0.0229				0.037				0.028	
ann		0.057			0.05			0.059				0.056				0.056				0.055	
east		0.035			0.038			0.032				0.033				0.042				0.036	
clin											0.021				0.021				0.022		
daph											0.027				0.029				0.025		
ames											0.0226				0.023				0.024		
Pressure	4±0.7	4±0.7			3.7±0.4			3.9±0.2				4.8±0.8				4±0.4				4±0.6	
Temp.	326±30	326±30			351±45			391±25				393±20				417±35				364±43	

The chemical formulae were calculated based on the number of oxygen atoms listed in the table and ignoring H_2O for hydrated minerals. Activities of end members were calculated with the program AX. Average pressure and temperature values were calculated with THERMOCALC. b.d.l is below detection limit.
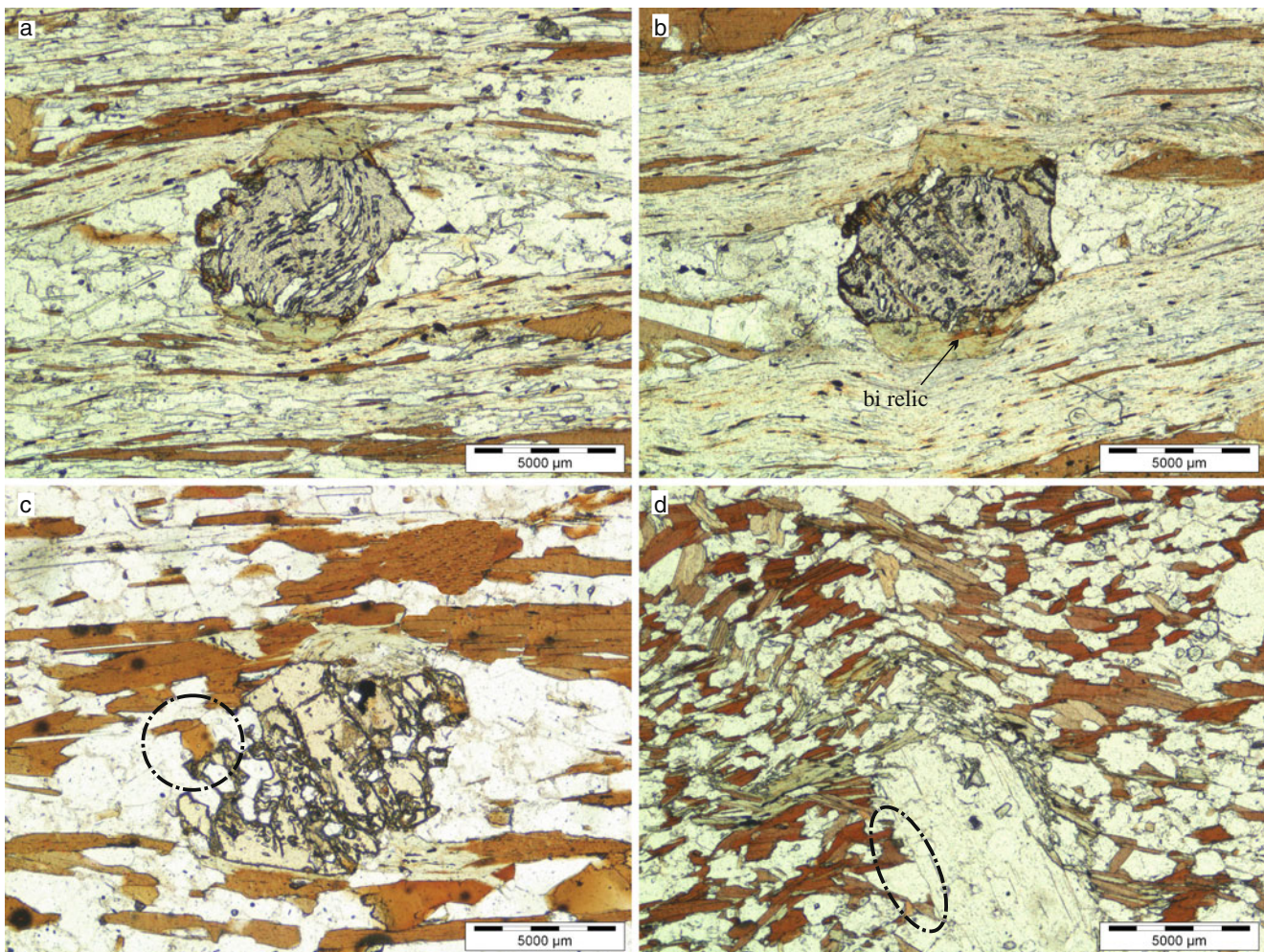
Fig. 2 Photomicrographs of different examples of polyphase strain caps. **a** Example from the central Himalayan metamorphic complex of Bhutan. Note that the spiral inclusion pattern within the garnet porphyroblast is partly consumed during the formation of the strain cap phase (see also Fig. 3). **b** Biotite relic in the strain cap region of Bhutan sample. The chlorite is found only in the strain cap region while the strain shadows are free of the micas. **c** Example from the Taba metamorphic complex of Sinai. The biotite lies in a direct contact with the staurolite porphyroblast at the strain shadow of Sinai sample but there is no chlorite between them. The staurolite porphyroblast is consumed by chlorite at the strain cap and by plagioclase at the strain shadow **d** Example from the Chugach metamorphic complex of southern Alaska. Note the biotite at left side of the porphyroblast is in direct contact with the muscovite but without any chlorite growth. The upper face of the muscovite porphyroblast is a convex face which may indicates that the muscovite starts to be consumed at the edge between two faces

forming the strain caps. The white mica has a chemical composition between muscovite and paragonite and occurs as 0.5×2 mm crystals. Biotite forms subhedral crystals (0.7×5 mm); compositionally it is between annite, phlogopite and eastonite. Quartz shows undulose extinction and lies interstitially between muscovite, biotite and garnet crystals. Garnet occurs as equidimensional grains (6×7 mm) and is with almandine rich. It has spiral inclusion patterns of quartz, sphene and biotite. Garnets usually have idiomorphic crystal faces on the sides where they touch the strain shadow but serrated edges where they are in contact with the strain caps (Fig. 2a and b). There is a slight variation in the FeO content between the region where the garnet rim touches that strain shadow (33.14–36.11 wt.%)

and the region where it is in contact with the strain cap (30.30–33.63 wt.%) (Table 1 and Fig. 4a). Compositional zoning and shape of the grain surfaces give the garnets the appearance that their rims were consumed subsequent to the formation of a concentric zoning pattern (Fig. 3a). The strain shadows are plagioclase-free areas, which are composed mainly of quartz with very small amounts of biotite and muscovite. Chlorite grains that exclusively grow in the strain caps are compositionally ripidolite with $X(\text{chl}) = \text{Fe}^{2+}/(\text{Fe}^{2+}+\text{Mg}^{2+}) = 0.569–0.577$ (Table 1). Chlorites often contain small mica relics which are aligned parallel to the metamorphic foliation (Fig. 2b). The relic grains have the same pleochroism as the mica grains in the foliated matrix. In addition chlorites contain small grains of muscovite with
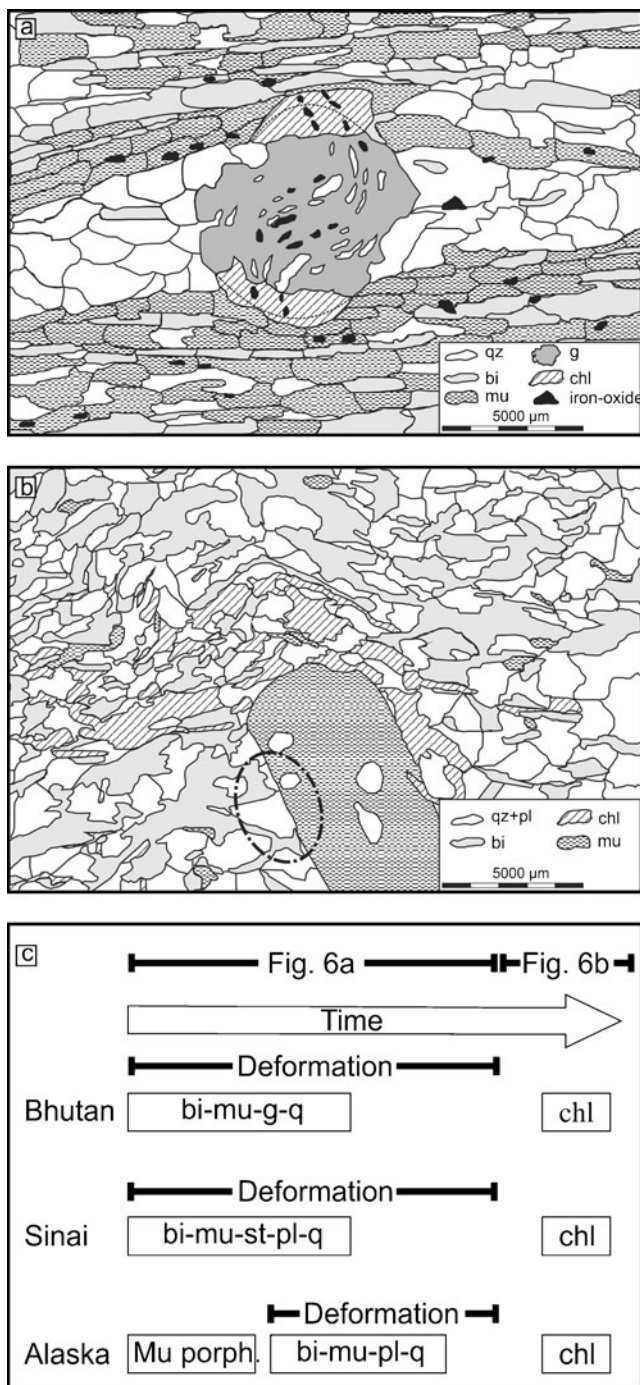
Fig. 3 Cartoons showing the main microstructural features of the strain caps in the Bhutan and Alaska examples. c Timing relationships between the deformation and the strain cap mineral growth as interpreted from the microstructural description

different pleochroism than the mica in the matrix. These small mica grains which are found along the chlorite cleavages parallel to crystal direction (001) have different chemistry (e.g. SiO_2, TiO_2 and K_2O) than the mica in the foliated matrix (Table 1). Careful comparative geothermobarometry between the strain cap region and the matrix

based on solving a set of reactions between mineral endmembers (Appendix 1a) showed that there is no local pressure variation between both regions within the error of the method. Both regions give P-T conditions around 6–7.2 kbar and 513–650°C (Table 1), corresponding to the estimates of Stüwe and Foster (2001).

The chosen sample from Sinai is a mica schist with coarse staurolite porphyroblasts and a matrix of biotite, muscovite, plagioclase, quartz and ilmenite (Fig. 2c). The metamorphic foliation is defined by parallel crystals of biotite, muscovite, plagioclase, quartz and ilmenite. The foliation is wrapped around the staurolite porphyroblasts. Both biotite and muscovite form crystals 0.05×0.6 mm in size with brownish and greenish white color, respectively. Quartz and plagioclase are anhedral to subhedral elongated crystals (0.2×0.5 mm). The plagioclase is oligoclase with Ca(pl) = Ca/(Ca+Na+K) = 0.21–0.25 (Table 2). The strain caps form around subhedral to euhedral (1×2 mm in size) staurolite porphyroblasts with cruciform twinning. The porphyroblasts are consumed by the chlorite growth at the strain cap region and by the plagioclase growth at the strain shadow region (Fig. 2c). The staurolite crystals contain inclusions of quartz, plagioclase and ilmenite. Minor biotite and muscovite can also be present as inclusions in staurolite. Long axes of the porphyroblasts are usually more or less parallel to the metamorphic foliation (Fig. 2c). Chlorite appears only in the strain caps and has a ripidolite composition. Chlorite cleavages are parallel to the metamorphic foliation while sub-microscopic ilmenite crystals grow perpendicular to these cleavages. The strain shadow regions are characterized by depletion in micas and enrichment in quartz and plagioclase. In few cases, the biotite of the strain shadow is in direct contact with the staurolite porphyroblasts (Fig. 2c). This observation is crucial for our interpretations below. Thermobarometry (Table 2 and Appendix 1b) indicates that this sample reached peak metamorphic conditions at pressures around 5.8–6.3 kbar and temperatures between 620 and 660°C with no difference in the conditions between the strain caps and the strain shadows.

Alaska sample contains coarse muscovite porphyroblasts embedded in a matrix of biotite, chlorite, plagioclase, quartz and apatite. The muscovites are colorless crystals with very weak pleochroism. Two types of muscovite were recognized; large euhedral porphyroblasts and small subhedral to euhedral crystals in the metamorphic foliation. The foliation is wrapped around the muscovite porphyroblasts. Small muscovite crystals (1×3 mm), biotite, quartz and plagioclase define the metamorphic foliation. Biotite is (1.5×5 mm) subhedral to euhedral crystals with perfect cleavages. Plagioclase forms colorless crystals attaining 1× 2.5 mm with albite and albite-Carlsbad twinning. Quartz forms anhedral to subhedral equant crystals (1.2×2 mm)

and it is characterized by wavy extinction. The muscovite porphyroblasts attain 5×18 mm in size. They have minor amount of quartz, plagioclase, muscovite and biotite as inclusions. The porphyroblasts have a random orientation within the ground matrix but they are constantly oblique to the metamorphic foliation (Fig. 2d). Crystal faces of the muscovite porphyroblasts which are against the strain cap are always convex (Fig. 2d and 3b). The strain shadows are composed of small muscovite crystals, biotite, plagioclase and quartz. The micas in the strain shadows lie in direct contacts with the muscovite porphyroblasts. The strain caps have the same mineralogical composition as the strain shadow, with the exception of the presence of chlorite with ripidolite composition. The chlorite grains are medium (0.3×1.5 mm), euhedral yellowish green crystals. The chlorites have biotite inclusions parallel to the chlorite cleavage. The strain cap and the strain shadow areas have the same range of pressure-temperature conditions (Table 3 and Appendix 1c) in the range 3.7–4.8 kbar and 326–417°C.

Interpreted timing relationships

For all three of the samples described above we infer similar timing relationships between metamorphism, deformation and the timing of formation of the strain caps. In the Bhutan and Sinai samples, porphyroblasts are interpreted to have grown syn-tectonically: In the Bhutan sample this is evidenced by spiral inclusion trails in garnet (Fig. 3a), in the Sinai samples staurolite is aligned in the foliation, but is itself undeformed. In both examples, strain caps formed after prophyroblast growth as the foliation is wrapped around the porphyroblast without penetrating them. Similarly, the strain caps in the Alaska sample also formed after porphyroblast growth, but the porphroblast itself formed prior to deformation: Muscovite porpyroblasts in the samples from Alaska are statically grown and rotated by the subsequent deformation (Fig. 3b). However, small muscovite crystals in the matrix apparently grew syntectonically. In all three samples, the absence of any deformation features in the chlorites in the strain cap region indicates that this mineral grew later as a post-tectonic phase (Fig. 3c). In the Alaska and Sinai samples, the strain cap chlorite appears to statically replace biotite and muscovite pseudomorphically. In the samples from Bhutan chlorite in the strain cap regions also partially replaces garnet. The convex faces of the muscovite against the strain cap (Fig. 2d and 3b) may indicate that muscovite consumption started at the edges of the porphyroblast. In Bhutan samples, the difference in the pleochroism and the chemistry (mu1* and mu3*; Table 1) between the small mica grains (along the chlorite cleavage) and the mica in the foliated matrix may indicate that the mica grains along the cleavages have a different origin than the relic grains

and the mica in the matrix. This observation is crucial for our discussion below.

Strain cap formation mechanism

There are at least three mechanisms that can explain the formation of new phases in the strain cap region: (a) the strain cap region may have experienced different P-T conditions from the matrix during the peak metamorphism, for example due to shear heating or local pressure gradients; (b) the strain cap region has different effective bulk composition from the surrounding matrix; (c) fluid flow that is preferentially focused parallel to the foliation planes causing only local adjustment to retrograde metamorphism in the strain cap region.

The first mechanism is easily excluded, because the new phase grown in the strain cap region (i.e. the chlorite) has a post-tectonic origin and grew later than the peak assemblage (Fig. 3c). Moreover, careful thermobarometry showed that the peak metamorphic conditions are uniform throughout the rock (Tables 1, 2, 3 and Appendix 1). The second mechanism is potentially viable as petrographic observations and element distribution maps (e.g. Fig. 4a) show that there are indeed differences in the local bulk composition between the strain cap regions and the strain shadow region: Most micas are in contact with the porphyroblasts only in the strain cap region so that the nutrients for the chlorite forming reaction are all present there. However, in two of the three investigated examples (Alaska and Sinai), micas are also observed in direct contact with the porphyroblasts in the strain shadow region (circled in Figs. 2c, d and 3b). Thus, the effective bulk composition required to form the chlorite is also locally presents in the strain shadow region—where chlorite never grows. Thus we exclude the local variation in effective bulk composition also as a formation mechanism to nucleate the strain cap mineral. However once the strain cap mineral had nucleated, the effective bulk composition plays an important role

Fig. 4 Thermodynamic pseudosections used for the interpretation of the strain cap formation. **a** Element distribution map showing the change in the effective bulk composition (e.g. FeO) around garnet porphyroblast. **b** P-T pseudosection of Sinai sample for average pelitic bulk (mole%); SiO_2: 73.18, Al_2O_3: 15.04, MgO: 6.53, FeO: 2.62, K_2O: 2.39. **c** Isobaric T-MH_2O pseudosection for the Sinai sample at 6 kbar for the same bulk composition of (**b**) and H_2O: 5.7–10.2. **d** P-T pseudosection for the Alaska sample. The bulk composition (mole%) is SiO_2: 68.00 Al_2O_3: 10.07, MgO: 6.09, FeO: 13.34, K_2O: 2.5. **e** P-T pseudosection for the strain cap region (Table 4) Bhutan sample. **f** P-T pseudosection for the strain shadow region (Table 4) Bhutan sample. **g** T-MH_2O pseudosection for the Bhutan sample at a pressure of 7 kbar for the same bulk composition of (e; strain cap composition) and H_2O: 1.18–10.62 (mole%). For all pseudosections the white arrows are the paths which will produce chlorite
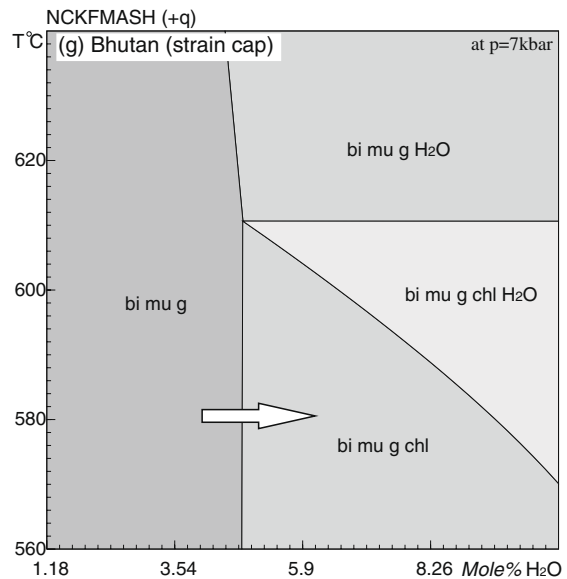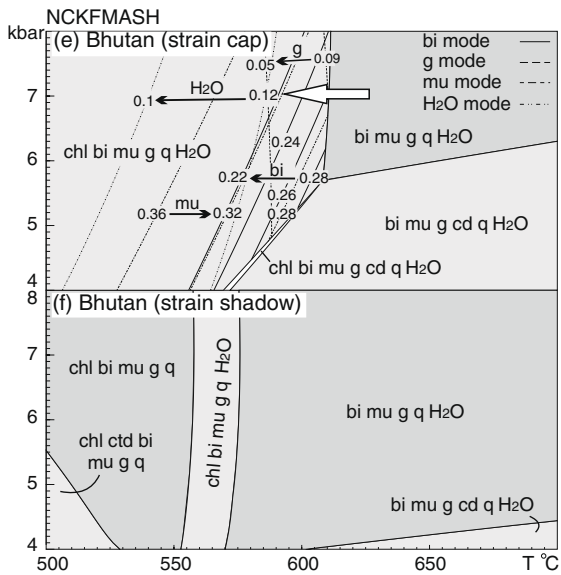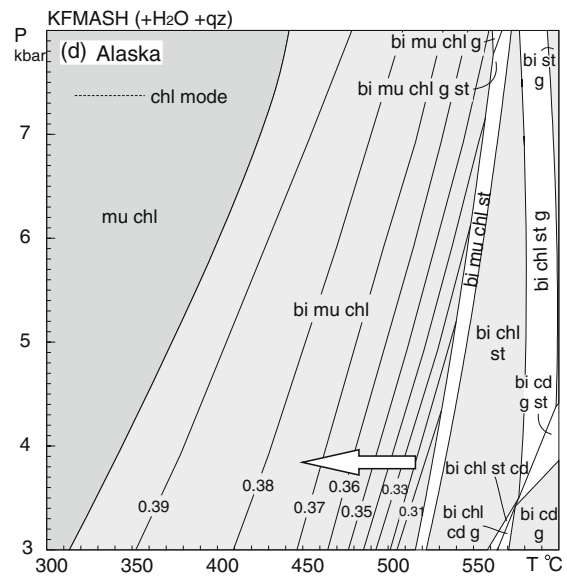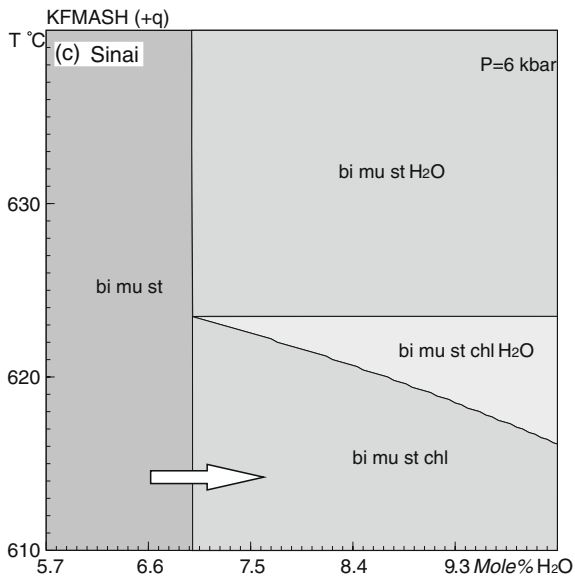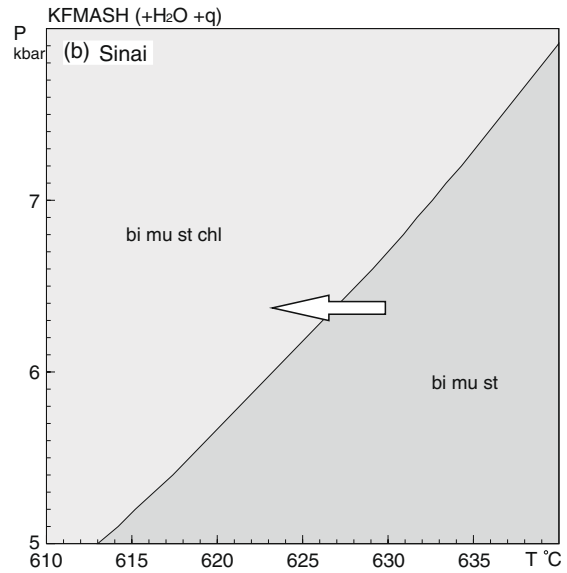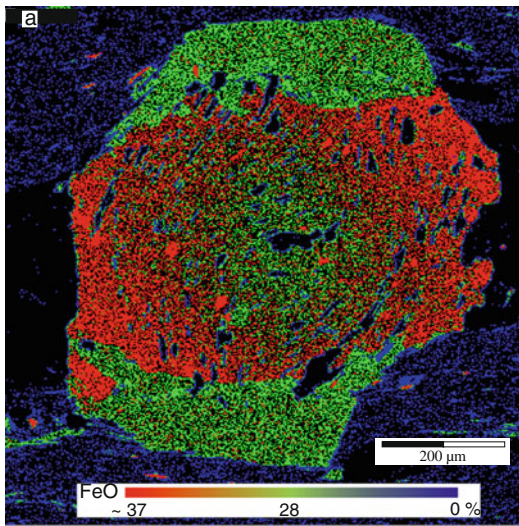
to grow these nucleuses so the growth of strain cap mineral will be discussed in more detail in the section of element diffusion below. Finally, the third mechanism—namely focused fluid flow along foliation planes—may be a possible model to explain the observations. In order to test this hypothesis we employ modeling using thermodynamic pseudosections.

Thermodynamic modeling

For our modeling we employ thermodynamic pseudosections. We construct thermodynamic pseudosections for several bulk compositions of the rocks described above to constrain the conditions of fluid flow around the porphyroblasts. As the strain caps of interest are a microstructure of millimeter scale and all occur in "normal" pelitic rocks, the XRF bulk chemistry will be not used here. Average pelitic bulk composition is used for Alaska sample (e.g. after Shaw 1956; Ague 1991; Mahar et al. 1997; Keller et al. 2005). For the Sinai sample we use the average bulk of Abu El-Enen (1995). These two samples (Alaska and Sinai) will be studied qualitatively. For more quantitative discussion the effective bulk composition of the Bhutan sample were calculated by $MBC_{1.7}$ (Abu-Alam and Stüwe 2009b, c) for both strain cap and strain shadow regions based on the volume proportions and the chemical composition of the phases (Table 4). The pseudosections were constructed using THERMOCALC 330 (Powell and Holland 1988) and the internally consistent dataset of Holland and Powell (1998). The following a-x models were used: biotite and

garnet (White et al. 2007); muscovite (Coggon and Holland 2002); cordierite and staurolite (Holland and Powell 1998) and chlorite (Holland et al. 1998). For Alaska and Sinai samples we constructed a P-T pseudosection (assuming the rocks were hydrated during their entire metamorphic evolution, i.e. with H_2O in excess) and a T-Mole% H_2O (henceforth called T-MH_2O) pseudosection at the pressure of interest to investigate changes in the hydration regime during cooling.

For the Sinai sample, the P-T and T-MH_2O pseudosections were constructed in the system KFMASH (Fig. 4b and c). The P-T pseudosection is characterized by presence of two fields: the divariant field (bi-mu-st-chl) at lower temperature condition and the trivariant field (bi-mu-st) at higher temperature condition showing that chlorite formation due to cooling is possible. At high H_2O concentration of the T-MH_2O pseudosection (Fig. 4c, constructed at pressure 6 kbar; Table 2), the divariant field (bi-mu-st-chl-H_2O) separates the trivariant assemblage (bi-mu-st-H_2O) at the higher temperature side from the assemblage (bi-mu-st-chl) at the lower temperature side. The chlorite-free assemblage (bi-mu-st) is stable at low water content (mole% H_2O: 5.7–7) and chlorite and ultimately also chlorite+water bearing assemblages become stable at successive stages of hydration. Thus, the chlorite in the Sinai samples can also form due to both processes: cooling and/or hydration. A P-T pseudosection for the sample from Alaska gives a similar conclusion: Although topologically somewhat different, the P-T pseudosection (Fig. 4d) shows that chlorite will grow on the expense of

Table 4 The effective bulk composition of Bhutan sample for the strain cap and strain shadow regions as calculated by Modal Bulk Composition ($MBC_{1.7}$) program (Abu-Alam and Stüwe 2009b, c)

Mineral	strain cap					strain shadow			
	g	bi	mu	chl	qz	g	bi	mu	qz
Volume (Mol.%)	17.79	17.96	26.55	12.03	25.67	5.22	1.25	0.49	93.02
SiO_2	37.06	35.89	47.08	24.14	100	37.9	35.76	46.57	100
TiO_2	0.24	2.96	0.65	0.29	–	0.17	2.69	0.58	–
Al_2O_3	20.70	19.02	34.44	22.00	–	20.89	18.28	35.43	–
Fe_2O_3	1.18	–	–	–	–	–	–	–	–
FeO	31.88	20.66	1.49	27.78	–	34.81	21.02	1.45	–
MnO	1.78	0.07	0.01	0.13	–	0.94	0.1	0.03	–
MgO	1.41	8.16	0.93	11.55	–	1.52	8.19	0.68	–
CaO	6.24	0.05	0.08	0.06	–	4.40	0.08	0.07	–
Na_2O	0.06	0.26	1.22	0.04	–	0.05	0.26	1.25	–
K_2O	0.01	10.09	10.28	0.16	–	0.03	9.98	10.11	–
H_2O	–	2.76	3.73	13.82	–	–	3.59	3.75	–
Eff. bulk comp.		Wt%	Mol%				Wt%	Mol%	
SiO_2		37.83	34.54				74.15	76.31	
Al_2O_3		23.74	12.77				8.75	5.3	
Fe_2O_3		0.17	0.06				0	0	
FeO		16.07	12.27				11.64	10.01	
MnO		0.31	0.24				0.26	0.23	
MgO		4.96	6.75				1.38	2.11	
CaO		0.95	0.93				1.17	1.29	
Na_2O		0.49	0.43				0.08	0.08	
K_2O		6.14	3.58				1.5	0.98	
H_2O		9.34	28.44				1.07	3.67	

The mineral chemistry is average of Table 1.

muscovite with cooling and a similar conclusion is true for hydration (not shown).

The *P-T* pseudosection for the Bhutan sample is modeled in the chemical system Na$_2$O-CaO-K$_2$O-FeO-MgO-Al$_2$O$_3$-SiO$_2$-H$_2$O (NCKFMASH). Figures 4e, g, 5 and 6 show the mineral equilibria with bulk composition corresponding to the bulk at the strain cap region (Table 4) while the lower part of the *P-T* pseudosection (Fig. 4f) shows the stability fields of the mineral assemblages with respect to the bulk composition at the strain shadow. It may be seen that a steep, near isothermal line separates chlorite-bearing assemblages at low temperatures from chlorite-free assemblages at high temperature. The temperature position of this line changes concerning the change in the bulk composition. At the strain cap, the boundary between chlorite-free and chlorite-bearing assemblages is around 610°C while this temperature is shifted to about 570°C at the strain shadow (Fig. 4e). Absence of chlorite at the strain shadow region indicates that the Bhutan rock did not pass the boundary between the chlorite-free and the chlorite-bearing assemblage (570°C) during the retrograde path. Garnet, biotite, muscovite and H$_2$O modes were added to the field (chl-bi-mu-g-q-H$_2$O). These modes show that garnet, biotite and H$_2$O stability decreases with temperature decrease (Fig. 4e) while the muscovite modes increase with temperature decrease. This explains the presence of small muscovite grains along the chlorite cleavage planes which have different pleochroism than the mica in the foliated matrix. In addition the decreasing in the H$_2$O mode indicates that the chlorite growth requires water consuming. By these modes, the strain cap formation reaction can be written in the system NCKFMASH+q as g+bi+H$_2$O=chl+mu. The transition from g-bi-mu assemblage to chl-bi-mu assemblage can be seen in qualitative KFM (K$_2$O, FeO, MgO) compatibility diagrams (Fig. 5). The KFASH+mu+q+H$_2$O grid (Fig. 5) simplifies the strain cap formation reaction to g+bi=chl (the thick line). The pseudosections suggest that one interpretation for the chlorite growth is simply that it grows due to cooling (arrow on Fig. 4e) and that its formation is largely independent of pressure.

To show the behavior of the Bhutan rock during hydration, a *T*-MH$_2$O pseudosection was calculated in the NCKFMASH system at a pressure of 7 kbar and bulk composition representing the strain cap region (Fig. 4g). The assemblage (bi-mu-g) is stable at low water content and over a wide range of temperatures (560–640°C). The chlorite bearing field bi-mu-g-chl is stable at low temperature condition (560–612°C) and H$_2$O content above 4.72 mole%. At the same H$_2$O range but with much higher temperature (>612°C), the assemblage bi-mu-g-H$_2$O becomes stable in the water saturated region. The assemblage bi-mu-g-chl-H$_2$O occurs at temperature range of 570–612°C and H$_2$O range of 4.72–10.62 mole%. The pseudo-

section suggests that isothermal hydration is a second possibility for the formation of the chlorite in the strain caps.

In summary, there is apparently no conclusive interpretation possible if the strain cap forming process is due to cooling or fluid infiltration. However, there is one observation that allows to rule out cooling: In two of the three chosen examples biotite is in contact with the porphyroblast without forming chlorite in a region outside the strain cap (Fig. 2c, d and 3b). In the samples from Sinai and Alaska, occasional biotite growth in the strain shadow region illustrates that the effective bulk composition is locally the same in the strains shadow and in the strain cap region. As there is no chlorite growing in the strain shadow—and the temperature history is undoubtedly the same for the entire thin section—we argue that cooling can be excluded as a unique formation mechanism of the strain cap chlorite. Thus fluid infiltration appears to be the dominant mechanism and we will discuss below if the amount of fluid can be quantified.

The role of fluid

Many authors discussed the role of the water during metamorphism (e.g. Guiraud et al. 2001). However, few authors have been able to quantify the amount of water that has infiltrated a given rock (e.g. Tenczer et al. 2006). Here, we suggest that the strain caps described above provide a unique opportunity to quantify the amount of fluid that has infiltrated the rock and how it varies around the microstructure described here. Figure 4c and g show that chlorite bearing fields can be reached from the chlorite-free fields simply by increasing the amount of water beyond 7 mole% and 4.72 mole%, respectively. However, both the chlorite absent field bi-mu-g and the chlorite present field bi-mu-g-chl are in the water undersaturated region of the phase diagram (Fig. 4g). Thus, it is difficult to see how fluids infiltrating the rock along grain boundaries could have reached the strain cap region without causing water undersaturated reaction further afield in the rock. We therefore suggest that the water infiltration must have been sufficient to bring the rock from the chlorite absent region bi-mu-g to the water saturated region bi-mu-g-chl-H$_2$O. This fluid infiltration by continuous metamorphic reaction allows to quantify the amount of fluid and, in fact, allows to infer a complete evolution for the water content of the rock.

Figure 6 shows the *T*-MH$_2$O pseudosection (at 7 kbar) for the spectacular strain caps of the Bhutan sample (Table 4) discussed above. This diagram can be used to illustrate the near-peak prograde heating path. Prograde dehydration during heating results in water loss and a path (black thick arrow in Fig. 6) that tracks along the water saturation line, because only a small proportion of free

Fig. 5 Enlargement of Fig. 4e. The inserts show KFASH (mu +q+H$_2$O) grid to show the reaction g+bi=chl (*thick line*) and two qualitative compatibility diagrams above and below the reaction. The compatibility diagrams are projected from quartz, staurolite, chloritoid and H$_2$O onto the plane K$_2$O-FeO–MgO. *Filled circles* show the bulk composition of the strain cap region
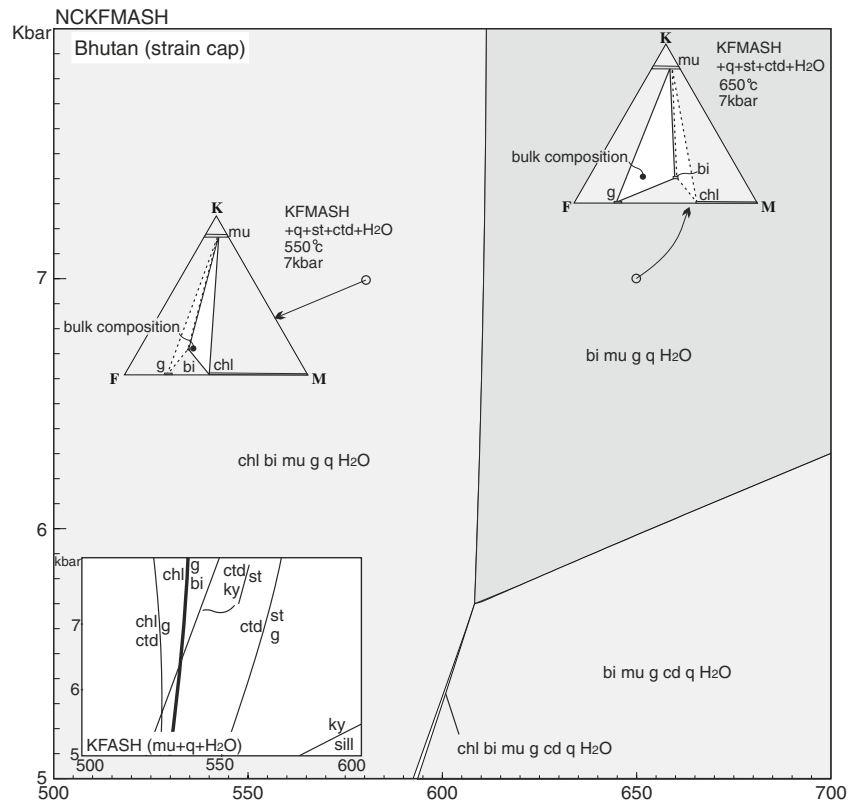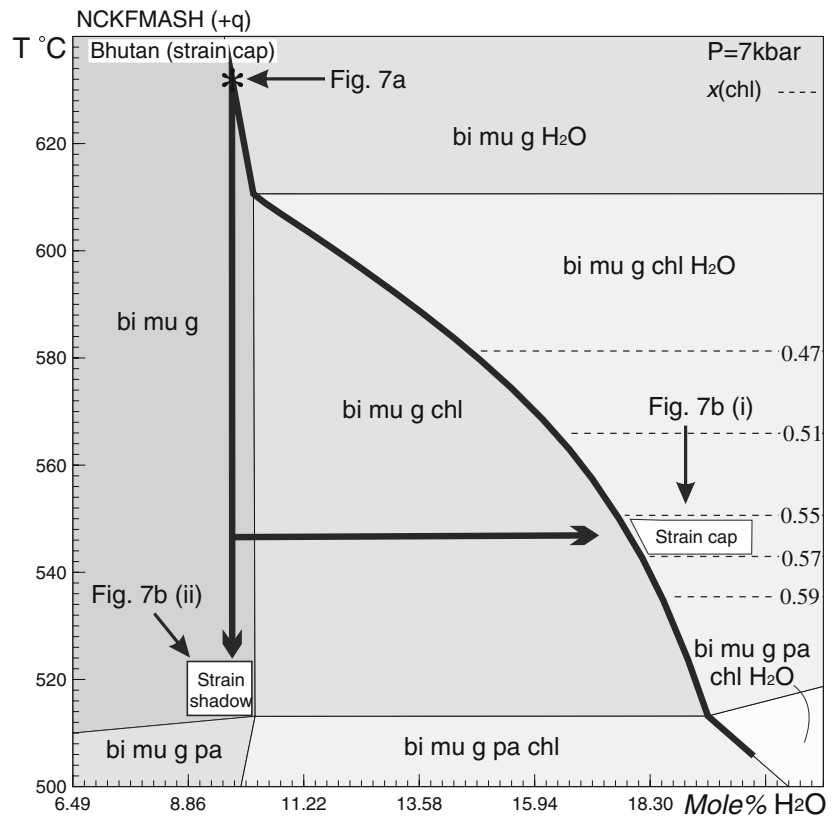

Fig. 6 *T*-MH$_2$O pseudosection for the strain cap region of Bhutan sample at 7 kbar and for the same bulk composition of Fig. 4e and H$_2$O: 6.49–20.66 (mole%). The *black arrow* is heating-dehydration path up to the *asterisk* followed by cooling path then hydration one. The (i) and (ii) are references to Fig. 7

water is likely to remain along grain boundaries (Guiraud et al. 2001) on traversing a series of phase fields with progressive dehydration, ultimately the peak assemblage bi-mu-g-H_2O. Following Stüwe and Foster (2001) and our own estimates, we assume that the metamorphic peak was reached within this field at around 630°C (as marked by the asterisk). Onset of cooling will "freeze" the water content of the assemblage to that of the metamorphic peak as the remaining free fluid is used up with incipient re-hydration. As such, the water content of the rock at the peak conditions is likely to have been just below 9.8 mole% H_2O. Subsequent cooling will preserve this water content (black down-temperature part of arrow in Fig. 6). At some stage during the cooling evolution fluid infiltration occurred and the dry assemblage was hydrated. In order to reach the fluid bearing field bi-mu-g-chl-H_2O, this hydration event could have occurred anywhere between 510°C and 610°C. The temperature at which this occurred can be closer constrained by the composition of the chlorite in the strain cap region: Contouring the relevant assemblage for X(chl) isopleths shows that the hydration is likely to have occurred around 550°C. This temperature constrains the additional amount of fluid infiltration to be about 8.5 mole% on top of the 9.8% of water locked in the solid phase assemblage. However, this fluid infiltration can only have occurred in the strain cap region, as the effective bulk composition defined by the contact paragenesis biotite-muscovite-garnet-quartz also occurs in other microstructural geometries without reaction to chlorite (Fig. 6 and Table 1). Such a strong gradient in fluid presence can only occur if the fluid flow occurred preferentially along the foliation only (Fig. 7). Once the fluid is added to the strain cap region and the chlorite starts to nucleate, elements start to diffuse from and to the strain cap region to allow chlorite growth. Elements diffusion process that occurs parallel to the chlorite growth is discussed below.

Elements diffusion

In the following section we will interpret the evolution of the strain cap microstructure using phase equilibria explicitly involving chemical potentials to show the diffusion of elements from and to the strain cap region. Quantitative μ-μ diagrams were calculated using THERMOCALC 330 and the internally consistent data sets of Holland and Powell (1998). Chemical potential relationships around the reaction g+bi=chl (the P-T grid of Fig. 5) are illustrated in the simpler chemical system KFMASH+quartz+H_2O for the minerals biotite, muscovite, garnet and chlorite. In this system the main controlling chemical potential is likely to be μ_{K2O} (White et al. 2008). In addition to K_2O, there will also be chemical potential gradients in MgO and FeO. The
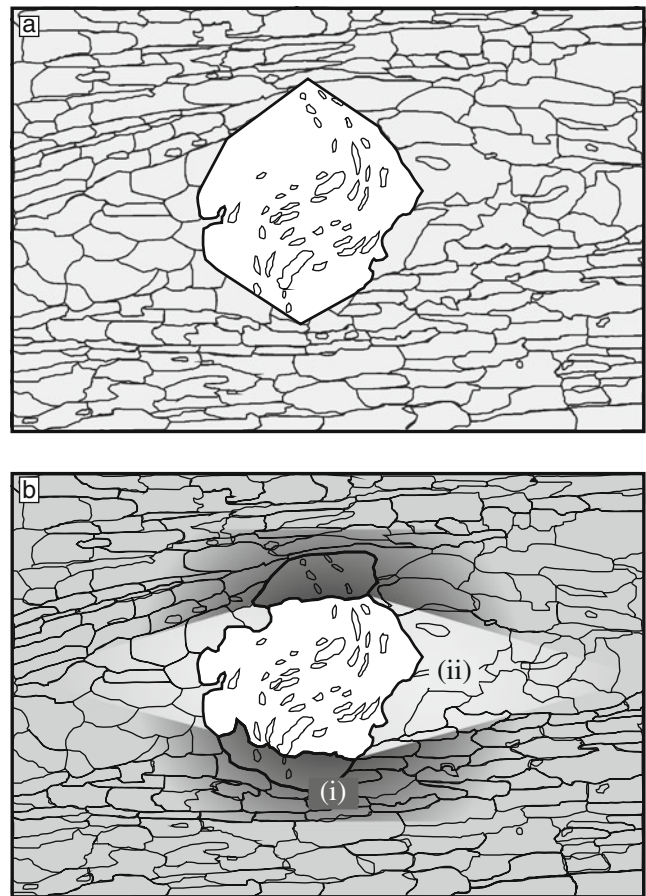
Fig. 7 Cartoon illustrates the focused fluid infiltration that caused the preferential growth of chlorite in the strain cap region. **a** is before chlorite growth and **b** is during chlorite growth. The shading corresponds to the concentration of fluid in the bulk rock with light grey=9.8 mole% of water, dark grey=18.3 mole% of water in bulk; medium grey=between 9.8 and 18.3 mole%

presence of quartz and H_2O as excess phases fixes μ_{SiO2} and μ_{H2O} to be constant across the diagrams. The value of μ_{Al2O3} varies across the diagram, and is effectively a passive variable, its value controlled via Gibbs-Duhem relationships. Allowing μ_{Al2O3} to vary freely between different equilibria without considering diffusion of Al_2O_3 is equivalent to considering Al_2O_3 to be immobile.

Figures 8a, b and c show the chemical potential relationships between K_2O, FeO and MgO at the low temperature side of the reaction g+bi=chl, at this condition the chl-bi-mu assemblage is the stable one (solid lines) while the dash lines are the metastable assemblage (g-bi-mu). The stable and the metastable points are connected by the line for the common assemblage bi-mu. At higher temperature conditions, the edge of the garnet grain along with coexisting muscovite and/or biotite would lie on the g-mu or g-bi lines or, most likely, at the g-bi-mu point (Fig. 8a, b and c). The interior of the garnet porphyroblast could lie within the garnet one phase field, or lie at its edge.
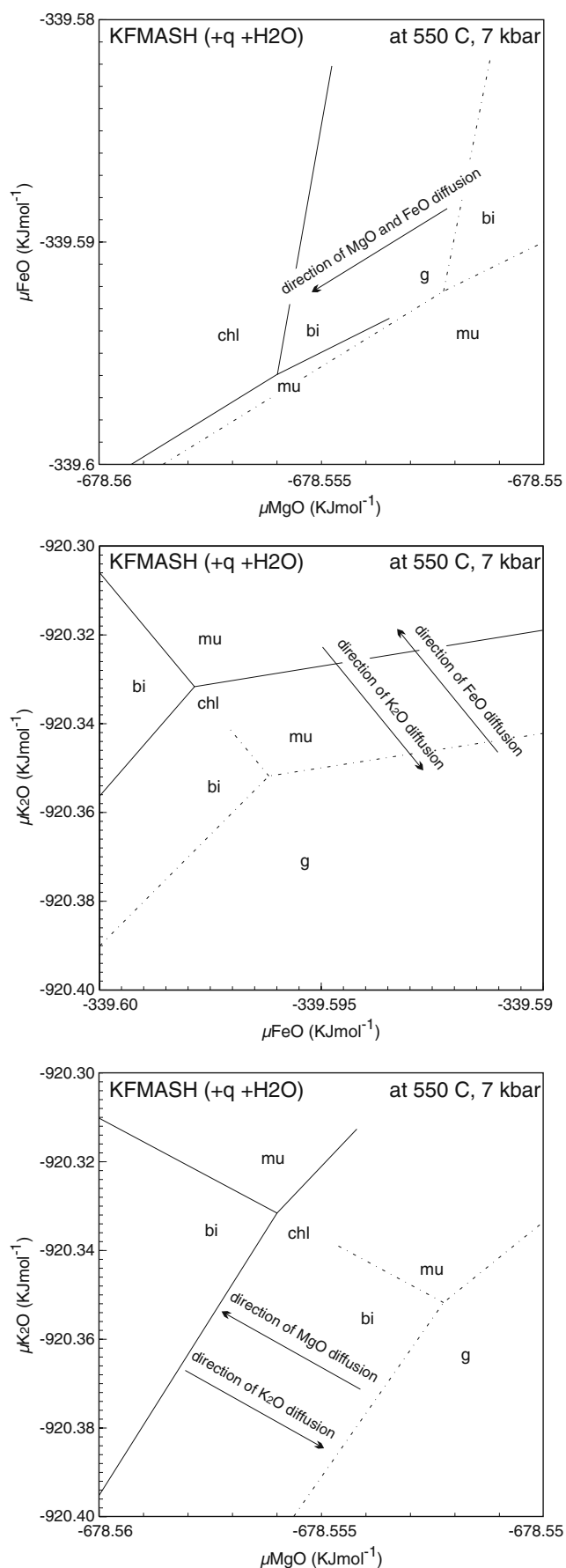
◀ **Fig. 8** Calculated μ-μ diagrams in KFMASH calculated at 550°C and 7 kbar. These P-T conditions are on the lower-T side of the reaction g+bi=chl. Each diagram is drawn with quartz and H_2O in excess. In each diagram the stable equilibria are shown as *solid lines* and the metastable equilibria are shown as *dashed lines*

The garnet-absent assemblage distal from the garnet grains would contain either biotite-muscovite prior the nucleation of chlorite or chlorite-biotite-muscovite if chlorite had nucleated. Figures 8b and c show that the chlorite-bearing lines and the bi-mu line, lie at higher μ_{K2O} than the corresponding garnet-bearing equilibria. Thus, there would tend to be diffusion of K_2O from the strain cap region to the garnet porphyroblast, once chlorite had nucleated. At the same time the FeO and the MgO diffuse from the garnet porphyroblast to the strain cap region (Fig. 8).

Consider an edge of garnet crystal located at contact with muscovite and biotite crystals, as replacement proceeds and the chlorite nucleated, the original point of the g-bi-mu will move along the bi-mu line towards the chl-bi-mu point. If the garnet grain at the contact with a biotite or a muscovite grain, the mineral equilibria lay at the line g-bi or g-mu. Once the chlorite nucleated the equilibria will move along the lines g-bi or g-mu till g-bi-mu point then along the bi-mu line toward the stable assemblage chl-bi-mu. While minimal addition of K_2O is involved in driving μ_{K2O} up (Fig. 8b and c) to the g-mu or to the g-bi lines if the newly exposed garnet lay within the garnet one phase field. Once the garnet grain is consumed, the gradient across the muscovite and biotite will be flattened out, with final position being the chl-bi-mu point. In case that the chlorite cannot be nucleated, the strain cap region will lose the K_2O toward the garnet porphyroblast and it will gain FeO and MgO from the garnet and the equilibria will be at the stable part of the bi-mu line in Fig. 8. However loss of K_2O from the cap region would occur regardless of where on the bi-mu line the cap region equilibria is located and this would rapidly drive the assemblage towards the chl-bi-mu point.

Conclusion

Strain caps are defined as a region that is depleted in quartz and enriched in micas occurring on opposite sides of the rigid body, in the quarters orthogonal to the strain shadow. In examples from the Bhutan Himalaya, the Chugach metamorphic complex of Alaska and the Taba metamorphic complex of Sinai chlorite grows exclusively in the strain cap region around porphyroblasts of garnet, muscovite and staurolite, respectively. Thermodynamic modeling shows that chlorite may form due to both, cooling or hydration but the microstructural position allows to conclude that the

polyphase strain caps must form due to focused fluid infiltration along the foliation planes of a pre-existing fabric postdating to the metamorphic peak. A local gradient in fluid concentration that includes at least 8.5 mole% difference in fluid mode of the bulk over a distance between strain cap and strain shadow must be maintained in order to avoid chlorite growth elsewhere in the microstructure. As such, our study presents a quantification of differences in fluid concentration infiltrating rocks on a centimeter scale.

Appendix 1

The independent reaction sets between the end-members as calculated by THERMOCALC. Sections a, b and c are for Bhutan, Sinai and Alaska, respectively.

Section a:

1) 3east + 6q = py + phl + 2mu
2) phl + east + 6q = py + 2cel
3) 2ann + mu + 6q = alm + 3fcel
4) py + 3east + 3fcel = alm + 3phl + 3mu
3) 2east + 6q = py + mu + cel
4) alm + 6east + 18q = 4py + 3mu + 3fcel
5) ann + 3east + 12q = 2py + mu + 3fcel
6) alm + 3east + 6q = 2py + ann + 2mu
7) 2alm + 3phl + 3east + 18q = 5py + 6fcel
8) ann + east + 6q = alm + 2cel
9) py + ann = alm + phl
10) 3ann + 3east + 18q = 2py + alm + 6fcel
11) 2phl + ames + 6q = py + 2cel + clin
12) alm + 6ann + 3ames + 18q = 4py + 6fcel + 3daph
13) 2py + 7fcel + daph = 4ann + 3east + 19q + 4H$_2$O
14) 2east + ames + 6q = py + 2mu + clin
15) 5alm + 2phl + 3ames + 6q = 6py + 2mu + 3daph
16) py + 6ann + 3ames + 18q = 4alm + 6fcel + 3clin
17) 3alm + 12fcel + 2clin = 7ann + 5east + 32q + 8H$_2$O
18) 4alm + 3fcel + 3ames = 4py + 3mu + 3daph
19) py + 3fcel = alm + 3cel
20) 6ann + 3ames + 18q = 2py + alm + 6cel + 3daph

Section b:

1) 18phl + 2mst + 13mu = 31east + 46q + 4H$_2$O
2) 2phl + mu + 2pa = 3east + 2ab + 3q + 2H$_2$O
3) 62phl + 6fst + 39mu = 8ann + 93east + 138q + 12H$_2$O
4) 30phl + 8ann + 7mu + 92pa = 45east + 92ab + 6fst + 80H$_2$O
5) 16phl + 8ann + 78pa + 21q = 24east + 78ab + 6fst + 66H$_2$O

6) 8ann + 62pa + 45q = 62ab + 6fst + 8mu + 50H$_2$O
7) 41east + 13clin + 47q = 41phl + 6mst + 40H$_2$O
8) phl + 3mu + clin = 4east + 7q + 4H$_2$O
9) 41mu + 18clin = 41east + 2mst + 80q + 68H$_2$O
10) 41mu + 31clin = 41phl + 8mst + 33q + 108H$_2$O
11) 33east + 47mu + 46clin = 80phl + 14mst + 156H$_2$O
12) 5phl + 2mst + 13cel = 18east + 46q + 4H$_2$O
13) 4mst + 41cel + 5clin = 41east + 127q + 28H$_2$O
14) 3cel + clin = 2phl + east + 7q + 4H$_2$O
15) 41cel + 18clin = 41phl + 2mst + 80q + 68H$_2$O
16) 80east + 47cel + 46clin = 127phl + 14mst + 156H$_2$O
17) 127mu + 46clin = 47east + 14mst + 80cel + 156H$_2$O
18) 41mu + 13clin + 47q = 6mst + 41cel + 40H$_2$O
19) 2mst + 18cel = 13east + 5mu + 46q + 4H$_2$O
20) 2mu + cel + clin = 3east + 7q + 4H$_2$O
21) 41ames + 47q = 6mst + 28clin + 40H$_2$O
22) 3mu + 5clin = 3phl + 4ames + 7q + 4H$_2$O
23) 47mu + 13clin + 33ames = 47phl + 14mst + 156H$_2$O
24) 28mu + 31ames + 13q = 28phl + 10mst + 104H$_2$O
25) 80mu + 46daph = 47ann + 14fst + 33fcel + 156H$_2$O
26) 41mu + 13daph + 47q = 6fst + 41fcel + 40H$_2$O
27) 2fst + 31fcel = 13ann + 18mu + 46q + 4H$_2$O
28) 4fcel + daph = 3ann + mu + 7q + 4H$_2$O
29) 41fcel + 18daph = 41ann + 2fst + 80q + 68H$_2$O
30) 41mu + 31daph = 41ann + 8fst + 33q + 108H$_2$O
31) 6fst + 93cel = 31phl + 8ann + 54mu + 138q + 12H$_2$O
32) 3cel + 2pa = phl + 2ab + 2mu + 3q + 2H$_2$O
33) 8ann + 45cel + 92pa = 15phl + 92ab + 6fst + 38mu + 80H$_2$O
34) 4phl + 8ann + 54pa + 57q = 54ab + 6fst + 12cel + 42H$_2$O
35) 3east + 3fcel = 2phl + ann + 3mu
36) 12phl + 2fst + 13fcel = 7ann + 18east + 46q + 4H$_2$O
37) 26phl + 2fst + 21mu = 39east + 8fcel + 46q + 4H$_2$O
38) phl + 3fcel = ann + 3cel
39) 3fcel + 2pa = ann + 2ab + 2mu + 3q + 2H$_2$O
40) mst + 4fcel = fst + 4cel
41) 13mst + 36fcel = 26east + 9fst + 10mu + 92q + 8H$_2$O
42) 2fst + 26cel = 13east + 5mu + 8fcel + 46q + 4H$_2$O
43) east + cel = phl + mu
44) 6fst + 62cel = 8ann + 31east + 23mu + 138q + 12H$_2$O
45) 23phl + 6fst + 39cel = 8ann + 54east + 138q + 12H$_2$O

Section c:

1) 3cel + ann = 3fcel + phl
2) 3fcel + 2pa = 2ab + 2mu + ann + 3q + 2H$_2$O
3) 4fcel + daph = mu + 3ann + 7q + 4H$_2$O
4) 12cel + 3daph = 3mu + 4phl + 5ann + 21q + 12H$_2$O
5) 9cel + daph = mu + 5fcel + 3phl + 7q + 4H$_2$O
6) 20fcel + 9clin = 5mu + 15phl + 4daph + 35q + 20H$_2$O
7) 4cel + clin = mu + 3phl + 7q + 4H$_2$O
8) 5cel + daph = 5fcel + clin
9) 5phl + 3daph = 5ann + 3clin

10) $9mu + 8phl + 3daph = 5ann + 12east + 21q + 12H_2O$

11) $3mu + phl + clin = 4east + 7q + 4H_2O$

12) $15mu + 5ann + 8clin = 20east + 3daph + 35q + 20H_2O$

13) $2ab + 5fcel + 2daph = 2pa + 5ann + 11q + 6H_2O$

14) $6ab + 15cel + 6daph = 6pa + 5phl + 10ann + 33q + 18H_2O$

15) $2ab + 15cel + 2daph = 10fcel + 2pa + 5phl + 11q + 6H_2O$

16) $2ab + 5fcel + 3clin = 2pa + 5phl + daph + 11q + 6H_2O$

17) $2ab + 5cel + 2clin = 2pa + 5phl + 11q + 6H_2O$

18) $9fcel + clin = mu + 5cel + 3ann + 7q + 4H_2O$

19) $12fcel + 3clin = 3mu + 5phl + 4ann + 21q + 12H_2O$

20) $20cel + 9daph = 5mu + 15ann + 4clin + 35q + 20H_2O$

21) $3fcel + 3east = 3mu + 2phl + ann$

22) $3fcel + 6pa + 4phl = 6ab + ann + 6east + 9q + 6H_2O$

23) $mu + 2pa + 2phl = 2ab + 3east + 3q + 2H_2O$

24) $8ab + 5mu + 3clin = 8pa + 5phl + 9q + 4H_2O$

25) $9cel + 14pa + 2phl = 14ab + 11mu + 3clin + 2H_2O$

26) $5cel + 6pa = 6ab + 5mu + clin + 2q + 2H_2O$

27) $3cel + 2pa = 2ab + 2mu + phl + 3q + 2H_2O$

28) $8ab + 5mu + 3daph = 8pa + 5ann + 9q + 4H_2O$

29) $9fcel + 14pa + 2ann = 14ab + 11mu + 3daph + 2H_2O$

30) $5fcel + 6pa = 6ab + 5mu + daph + 2q + 2H_2O$

31) $45cel + 70pa + 10ann = 70ab + 55mu + 9clin + 6daph + 10H_2O$

32) $2ab + 5cel + 3daph = 2pa + 5ann + clin + 11q + 6H_2O$

33) $2ab + 15fcel + 2clin = 10cel + 2pa + 5ann + 11q + 6H_2O$

34) $6ab + 15fcel + 6clin = 6pa + 10phl + 5ann + 33q + 18H_2O$

35) $5ann + 3ames = 2phl + 3east + 3daph$

36) $phl + ames = east + clin$

References

Abu-Alam TS, Stüwe K (2009a) Exhumation during oblique transpression: an example from the Feiran-Solaf region, Egypt. J Metamorph Geol 27:439–459

Abu-Alam TS, Stüwe K (2009b) MBC (1.7): a visual basic code to calculate bulk composition of rocks from chemistry and volume proportions of the phases. Geol Soc America (GSA)-Abstract with programs 41, pp 500

Abu-Alam TS, Stüwe K (2009c) The MBC (1.7): a visual basic program to calculate bulk composition of rocks from chemistry and the volume proportions of the phases. Mitt Österr Mineral Ges 155, p 17

Abu-Alam TS, Stüwe K, Hauzenberger C (2010) Calc-silicates from Wadi Solaf region, Sinai, Egypt. J Afr Earth Sci 58:475–488

Abu El-Enen MM (1995) Geological, geochemical and mineralogical studies on the metamorphic rocks between Wadi Um-Maghra and Wadi Tweiba area, southeastern Sinai, Egypt. Ph.D. thesis, Mansoura Univ, Egypt. 172 pp

Abu El-Enen MM, Zalata AA, El-Metwally AA, Okrusch M (1999) Orthogneisses from the Taba metamorphic belt, SE Sinai, Egypt: witnesses for granitoid magmatism at an active continental margin. N Jahrb Mineral Abh 175:53–81

Abu El-Enen MM, Will TM, Okrusch M (2004) P–T evolution of the Pan-African Taba metamorphic belt, Sinai, Egypt: constraints from metapelitic mineral assemblages. J Afr Earth Sci 38:59–78

Ague JJ (1991) Evidence for major mass transfer and volume strain during regional metamorphism of pelites. Geology 19:855–858

Barker F, Farmer GL, Ayuso RA, Plafker G, Lull JS (1992) The 50 Ma granodiorite of the eastern Gulf of Alaska: Melting in an accretionary prism in the forearc. J Geophys Res 97:6757–6778

Bruand E, Gasser D, Stüwe K, Beyssac O (2010) Metamorphism of the Chugach Metamorphic Complex, (Alaska). New pressure estimates question the ridge subduction context. Geophys Res Abst 12:EGU2010–12235

Coggon R, Holland TJB (2002) Mixing properties of phengitic micas and revised garnet-phengite thermobarometers. J Metamorph Geol 20:683–696

Cosca MA, Shimron A, Caby R (1999) Late Precambrian metamorphism and cooling in the Arabian-Nubian Shield: petrology and $^{40}Ar/^{39}Ar$ geochronology of metamorphic rocks of the Elat area (southern Israel). Precambrian Res 98:107–127

Dasgupta S, Ganguly J, Neogi S (2004) Inverted metamorphic sequence in the Sikkim Himalayas: crystallization history, P–T gradient and implications. J Metamorph Geol 22:395–412

Eliwa HA, Abu El-Enen MM, Khalaf IM, Itaya T, Murata M (2008) Metamorphic evolution of Neoproterozoic metapelites and gneisses in Sinai, Egypt: insights from petrology, mineral chemistry and K–Ar age dating. J Afr Earth Sci 51:107–122

England P, Le Fort P, Molnar P, Pecher A (1992) Heat sources for Tertiary metamorphism and anatexis in the Annapurna-Manaslu region, Central Nepal. J Geophys Res 97:2107–2128

Etchecopar A, Malavieille J (1987) Computer models of pressure shadows: a method for strain measurement and shear-sense determination. J Struct Geol 9:667–677

Farris DW, Paterson SR (2007) Physical contamination of silicic magmas and fractal fragmentation of xenoliths in Paleocene plutons on Kodiak Island, AK. Can Mineral 45:107–129

Farris DW, Paterson SR (2009) Subduction of a segmented ridge along a curved continental margin: variations between the western and eastern Sanak-Baranof belt, southern Alaska. Tectonophysics 464:100–117

France-Lanord C, Le Fort P (1988) Crustal melting and granite genesis during the Himalayan collision orogenesis. Trans R Geol Soc Edinburgh 79:183–195

Gansser A (1964) Geology of the Himalayas. Wiley Interscience, London

Grujic D, Casey M, Davidson C, Hollister L, Kündig R, Pavlis T (1996) Ductile extrusion of the higher Himalayan Crystalline in Bhutan: evidence from quartz microfabrics. Tectonophysics 260:21–44

Guiraud M, Powell R, Rebay G (2001) H_2O in metamorphism and unexpected behaviour in the preservation of metamorphic mineral assemblages. J Metamorph Geol 19:445–454

Heimann A, Eyal Y, Eyal M, Foland KA (1995) Thermal events and low temperature alteration in the Precambrian schistose dykes and their host rocks in the Elat area, southern Israel: $^{40}Ar/^{39}Ar$ geochronology. In: Baer G, Heimann A (eds) Physics and Chemistry of Dykes. Balkema, Rotterdam, pp 281–292

Hill M, Morris J, Whelan J (1981) Hybrid granodiorites intruding the accretionary prism, Kodiak, Shumagin and Sanak Islands, Southwest Alaska. J Geophys Res 86:10569–10590

Hodges KV, Bowring S, Davidek K, Hawkins D, Krol M (1988) Evidence for rapid displacement on Himalayan normal faults and

the importance of tectonic denudation in the evolution of mountain ranges. Geology 26:483–486

Hodges KV, Parrish RR, Searle MP (1996) Tectonic evolution of the central Annapurna Range, Nepalese Himalayas. Tectonics 15:1264–1291

Holland TJB, Powell R (1998) An internally consistent thermodynamic dataset for phases of petrological interest. J Meta Geol 16:309–343

Holland TJB, Baker JM, Powell R (1998) Mixing properties and activity-composition relationships of chlorites in the system MgO-FeO-Al_2O_3-SiO_2-H_2O. Eur J Mineral 10:395–406

Hubbard MS (1989) Thermobarometric constraints on the thermal history of the Main Central thrust zone and Tibetan slab, eastern Nepal Himalaya. J Metamorph Geol 7:19–30

Hubbard MS, Harrison TM (1989) ^{40}Ar/^{39}Ar constraints on deformation and metamorphism in the Main Central Thrust zone and Tibetan Slab, eastern Nepal Himalaya. Tectonics 8:865–880

Hudson T, Plafker G (1982) Paleogene metamorphism of an accretionary flysch terrane, eastern Gulf of Alaska. Geol Soc Amer Bull 93:1280–1290

Keller LM, Abart R, Schmid SM, De Capitani C (2005) Phase relations and chemical composition of phengite and paragonite in pelitic schists during decompression: a case study from the Monte Rosa Nappe and Camughera–Moncucco Unit, Western Alps. J Petrol 46:2145–2166

Kröner A, Eyal M, Eyal Y (1990) Early Pan-African evolution of the basement around Elat, Israel, and Sinai Peninsula revealed by single-zircon evaporation dating, and implication for crustal accretion rates. Geology 18:545–548

Le Fort P (1975) Himalaya: the collided range. Present knowledge about the continental arc. Am J Sci 275A:1–44

Le Fort P (1981) Manaslu leucogranite: a collision signature of the Himalaya. A model for its genesis and emplacement. J Geophys Res 86:10545–10568

Mahar EM, Baker JM, Powell R, Holland TJB, Howell N (1997) The effect of Mn on mineral stability in metapelites. J Metamorph Geol 15:223–238

Moore JC, Byne T, Plumley PW, Reid M, Gibbons H, Coe RS (1983) Paleogene evolution of the Kodiak Islands, Alaska: consequences of ridge-trench interaction in a more southerly latitude. Tectonics 2:265–293

Passchier CW, Trouw RAJ (1996) Micro-tectonics. Springer Verlag, New York, 289

Passchier CW, Trouw RAJ (2005) Micro-tectonics. Springer Verlag, New York, 366

Plafker G, Moore JC, Winkler GR (1994) Geology of the southern Alaska margin: the Geology of North America, G-1. The Geology of Alaska. Geol Soc Am 12:389–449

Powell R, Holland TJB (1988) An internally consistent thermodynamic dataset with uncertainties and correlations: 3. Application, methods, work examples and a computer program. J Metamorph Geol 6:173–204

Shaw DM (1956) Geochemistry of pelitic rocks. Part III: Major elements and general geochemistry. Bull Geol Soc Am 67:919–934

Shimron AE (1980) Proterozoic island arc volcanism and sedimentation in Sinai. Precambrian Res 12:437–458

Sisson VB, Hollister LS (1988) Low-pressure facies series metamorphism in an accretionary sedimentary prism, southern Alaska. Geology 16:358–361

Sisson VB, Hollister LS, Onstott TC (1989) Petrologic and age constraints on the origin of a low-pressure/high-temperature metamorphic complex, southern Alaska. J Geophys Res 94:4392–4410

Sisson VB, Poole PR, Harris NR, Burner HC, Pavlis TL, Copeland P, Donelick RA, McLelland WC (2003) Geochemical and geochronologic constraints for the genesis of tonalite-trondhjemite suite and associated mafic intrusive rocks in the eastern Chugach Mountains, Alaska: a record of ridge-transform subduction: geology of a transpressional orogen developed during ridge-trench interaction along the North Pacific Margin. Geol Soc Am Spec Pap 371:293–326

Stüwe K, Foster D (2001) ^{40}Ar/^{39}Ar, pressure, temperature and fission track constraints on the age and nature of metamorphism around the main central thrust in the eastern Bhutan Himalaya. J Asia Earth Sci 19:85–95

Takagi H, Ito M (1988) The use of asymmetric pressure shadows in mylonites to determine the sense of shear. J Struct Geol 10:347–360

Tenczer V, Stüwe K, Barr TD (2001) Pressure anomalies around cylindrical objects in simple shear. J Struct Geol 23:777–788

Tenczer V, Powell R, Stüwe K (2006) Evolution of H_2O content in a polymetamorphic terrane: the Plattengneiss Shear Zone (Koralpe, Austria). J Metamorph Geol 24:281–295

Trouw RAJ, Tavares FM, Robyr M (2008) Rotated garnets: a mechanism to explain the high frequency of inclusion trail curvature angles around 90° and 180°. J Struct Geol 30:1024–1033

Vannay JC, Hodges KV (1996) Tectonometamorphic evolution of the Himalayan metamorphic core between Annapurna and Dhaula-giri, central Nepal. J Metamorph Geol 14:635–656

Vidal P, Cocherie A, Le Fort P (1982) Geochemical investigations of the origin of the Manaslu leucogranite (Himalaya, Nepal). Geochim Cosmochim Acta 46:2279–2292

White RW, Powell R, Holland TJB (2007) Progress relating to calculation of partial melting equilibria for metapelites. J Metamorph Geol 25:511–527

White RW, Powell R, Baldwin JA (2008) Calculated phase equilibria involving chemical potentials to investigate the textural evolution of metamorphic rocks. J Metamorph Geol 26:181–198